

High-mobility three-atom-thick semiconducting films with wafer-scale homogeneity

Kibum Kang^{1*}, Saien Xie^{2*}, Lujie Huang¹, Yimo Han², Pinshane Y. Huang², Kin Fai Mak^{3,4}, Cheol-Joo Kim¹, David Muller^{2,3} & Jiwoong Park^{1,3}

The large-scale growth of semiconducting thin films forms the basis of modern electronics and optoelectronics. A decrease in film thickness to the ultimate limit of the atomic, sub-nanometre length scale, a difficult limit for traditional semiconductors (such as Si and GaAs), would bring wide benefits for applications in ultrathin and flexible electronics, photovoltaics and display technology^{1–3}. For this, transition-metal dichalcogenides (TMDs), which can form stable three-atom-thick monolayers⁴, provide ideal semiconducting materials with high electrical carrier mobility^{5–10}, and their large-scale growth on insulating substrates would enable the batch fabrication of atomically thin high-performance transistors and photodetectors on a technologically relevant scale without film transfer. In addition, their unique electronic band structures provide novel ways of enhancing the functionalities of such devices, including the large excitonic effect¹¹, bandgap modulation¹², indirect-to-direct bandgap transition¹³, piezoelectricity¹⁴ and valleytronics¹⁵. However, the large-scale growth of monolayer TMD films with spatial homogeneity and high electrical performance remains an unsolved challenge. Here we report the preparation of high-mobility 4-inch wafer-scale films of monolayer molybdenum disulphide (MoS₂) and tungsten disulphide, grown directly on insulating SiO₂ substrates, with excellent spatial homogeneity over the entire films. They are grown with a newly developed, metal-organic chemical vapour deposition technique, and show high electrical performance, including an electron mobility of 30 cm² V⁻¹ s⁻¹ at room temperature and 114 cm² V⁻¹ s⁻¹ at 90 K for MoS₂, with little dependence on position or channel length. With the use of these films we successfully demonstrate the wafer-scale batch fabrication of high-performance monolayer MoS₂ field-effect transistors with a 99% device yield and the multi-level fabrication of vertically stacked transistor devices for three-dimensional circuitry. Our work is a step towards the realization of atomically thin integrated circuitry.

Existing growth methods for large-scale monolayer TMDs have so far produced materials with limited spatial uniformity and electrical performance. For instance, the sulphurization of metal or metal compounds only provides control over the average layer number, producing spatially inhomogeneous mixtures of monolayer, multi-layer and no-growth regions^{16,17}. Although chemical vapour deposition (CVD) based on solid-phase precursors (such as MoO₃, MoCl₅ or WO₃)^{18–23} has shown better thickness control on a large scale, the electrical performance of the resulting material, which is often reported from a small number of devices in selected areas, fails to show spatially uniform high carrier mobility.

Here we report the growth of semiconducting monolayer films of MoS₂ and tungsten disulphide (WS₂) on silicon oxide on a 4-inch wafer scale, with both excellent electrical performance and structural continuity, maintained uniformly over the entire films. Figure 1 presents our continuous TMD monolayer films and shows their wafer-scale homogeneity and intrinsic optical properties. The colour photos of MoS₂ (Fig. 1a; greenish yellow) and WS₂ (Fig. 1b; yellow) films

grown on a transparent 4-inch fused silica wafer show that the TMD grown region (right half) is uniform over the whole substrate and clearly distinguishable from the bare silica substrate (left half). The optical absorption, photoluminescence and Raman spectra measured from our films show characteristics unique to monolayer MoS₂ and WS₂, respectively (Fig. 1d–f). All of these measured spectra have the same peak positions as in exfoliated monolayer samples (denoted by diamonds)^{13,24–26}, regardless of the location of the measurements within our films (Supplementary Fig. 1). The X-ray photoelectron spectra taken from our monolayer MoS₂ film show almost identical features to those of bulk single crystal with a low level of defects, further confirming the precise chemical composition and the high quality of our MoS₂ film (Supplementary Fig. 2).

Figure 1c shows a photo of a MoS₂ film grown on a 4-inch SiO₂/Si wafer. The monolayer film was patterned using standard photolithography and oxygen plasma etching to form MoS₂-covered squares (dark, 6 mm wide) with an array of 3 μm holes. An enlarged, normalized optical reflection image (Fig. 1h) displays a homogeneous reflection contrast for the entire MoS₂-covered region, confirming uniform monolayer growth everywhere with no gaps. In addition, Fig. 1g shows a scanning electron microscope (SEM) image of an array of fully suspended monolayer MoS₂ membranes (2 μm in diameter) fabricated by transferring our metal-organic chemical vapour deposition (MOCVD)-grown film onto a SiN grid with holes. Its high fabrication yield (>99.5%) suggests mechanical strength and continuity of the film. The widefield photoluminescence images of these films (insets to Fig. 1g, h) show strong, spatially uniform photoluminescence signals, further confirming that they are continuous monolayer MoS₂, with its high quality maintained even after patterning or transfer. The same spatial uniformity was seen in the optical reflection and photoluminescence images of a monolayer WS₂ film that was similarly grown and patterned (Fig. 1i). Together, the data in Fig. 1 confirm that our MoS₂ and WS₂ films are continuous monolayers, spatially uniform over the entire 4-inch growth substrates with intrinsic optical properties. Below, using MoS₂ as the main example, we discuss the growth (Fig. 2) and the excellent electrical properties (Fig. 3) of these MOCVD-grown films.

Figure 2a schematically explains our MOCVD growth, where we only use gas-phase precursors of Mo(CO)₆, W(CO)₆, (C₂H₅)₂S and H₂, all diluted in argon as a carrier gas (see Supplementary Methods). The concentration of each reactant can be precisely controlled during the entire growth time by regulating the partial pressure (P_X) of each reactant X. Thus our setup offers an ideal environment for maximizing the areal coverage of the monolayer and for engineering the film structure by controlling the nucleation density and intergrain stitching. Figure 2 summarizes our key findings.

First, our MoS₂ film is grown in the layer-by-layer growth mode, which is ideal for uniform layer control over the large scale. Figure 2c plots the areal coverage of monolayer (θ_{1L}) and multilayer ($\theta_{\geq 2L}$; mostly bilayer) regions measured from our MoS₂ grown on SiO₂/Si;

¹Department of Chemistry and Chemical Biology, Cornell University, Ithaca, New York 14853, USA. ²School of Applied and Engineering Physics, Cornell University, Ithaca, New York 14853, USA. ³Kavli Institute at Cornell for Nanoscale Science, Ithaca, New York 14853, USA. ⁴Laboratory of Atomic and Solid State Physics, Cornell University, Ithaca, New York 14853, USA.

*These authors contributed equally to this work.

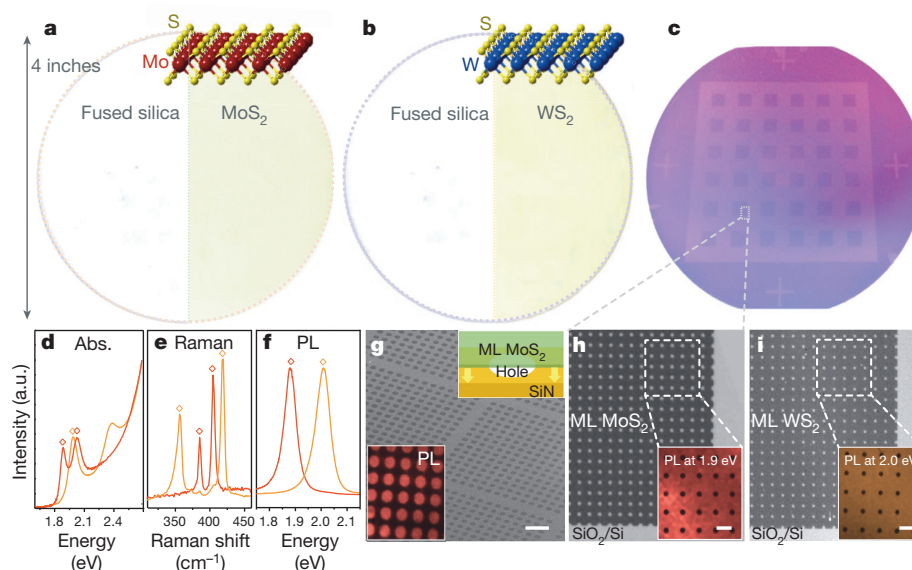


Figure 1 | Wafer-scale monolayer TMD films. **a, b**, Photographs of monolayer MoS₂ (**a**) and WS₂ (**b**) films grown on 4-inch fused silica substrates, with diagrams of their respective atomic structures. The left halves show the bare fused silica substrate for comparison. **c**, Photograph of patterned monolayer MoS₂ film on a 4-inch SiO₂/Si wafer (the darker areas are covered by MoS₂). **d**, Optical absorption spectra of MOCVD-grown monolayer MoS₂ (red line) and WS₂ (orange line) films in the photon energy range from 1.6 to 2.7 eV. **e**, Raman spectra of as-grown monolayer MoS₂ and WS₂, normalized to the silicon peak intensity. **f**, Normalized photoluminescence spectra of

as-grown monolayer MoS₂ and WS₂. The peak positions in **d–f** are consistent with those seen from exfoliated samples (diamonds). **g**, SEM image and photoluminescence (PL) image (bottom inset, at 1.9 eV) of monolayer (ML) MoS₂ membranes suspended over a SiN TEM grid with 2 μm holes (a diagram of the suspended film is shown in the top inset). Scale bar, 10 μm. **h, i**, Optical images (normalized to the bare substrate region) of patterned monolayer MoS₂ (**h**) and WS₂ (**i**) on SiO₂, taken from the wafer-scale patterned films. The insets show photoluminescence images at 1.9 eV (**h**) and 2.0 eV (**i**). Scale bars, 10 μm.

Fig. 2b shows optical images at different growth times, revealing the initial nucleation on the SiO₂ surface ($t = 0.5t_0$), subsequent monolayer growth near ($0.8t_0$) and at the maximum monolayer coverage (t_0), followed by nucleation mainly at grain boundaries ($1.2t_0$) and bilayer growth ($2t_0$). We observed no nucleation of a second layer while the first layer was forming ($\theta_{\geq 2L} \approx 0$ when $t < t_0$), producing an optimal growth time t_0 near full monolayer coverage ($\theta_{1L} \approx 1$). Additional photoluminescence and electron microscope images taken after different growth times further suggested that the edge attachment was the main mechanism for the monolayer growth after nucleation and that the neighbouring monolayer grains were uniformly connected by tilt grain boundaries with enhanced photoluminescence¹⁹ at $t = t_0$ (see Supplementary Notes and Supplementary Figs 3 and 4). The standard thin-film growth model²⁷ suggests that this growth mode is effective below a certain deposition rate of the growth species, above which it suggests a different mode that forms thicker islands. Indeed, the layer-by-layer growth of MoS₂ film was observed only when we applied a low partial pressure ($P_{\text{Mo}} \approx 10^{-4}$ Torr in Fig. 2b, c) of Mo vapour (produced by the thermal decomposition of Mo(CO)₆; see Supplementary Notes and Supplementary Fig. 5) in the presence of excess (C₂H₅)₂S. In contrast, the growth at a higher P_{Mo} was no longer in the layer-by-layer growth mode, instead simultaneously producing a mixture of monolayer, multilayer and no-growth regions (Supplementary Fig. 6). For the uniform monolayer growth over a large substrate, it is thus important to maintain a low P_{Mo} constantly over the entire growth region and over time, the key technical capability provided by our MOCVD setup (see Supplementary Fig. 7 for the spatially homogeneous monolayer nucleation on a multi-inch scale).

Second, the grain structure of our MoS₂ film, including the average grain size and the intergrain connection, depends sensitively on the concentrations of H₂, (C₂H₅)₂S as well as residual water. As a representative example, Fig. 2d shows the two main effects of H₂, whose presence is necessary for removing carbonaceous species generated during the MOCVD growth: the average grain size increases from hundreds of nanometres to more than 10 μm with decreasing H₂ flow, and the MoS₂ grains grown under higher H₂ flow (Fig. 2d, right image)

have mostly perfect triangular shapes without merging with neighbouring grains, a trend that disappears with lower H₂ flow (left and middle images). These observations are consistent with the H₂-induced decomposition of (C₂H₅)₂S (increasing nucleation due to hydrogenolysis)²⁸ and the etching of the MoS₂ (preventing intergrain connection)²⁹ as reported previously. (For further discussion on the effects of (C₂H₅)₂S and water, see Supplementary Notes and Supplementary Fig. 6.) To grow continuous monolayer MoS₂ with a large grain size and high-quality intergrain stitching, we thus flowed optimal amounts of H₂ and (C₂H₅)₂S and dehydrated the growth environment.

The darkfield transmission electron microscope (DF-TEM) and annular darkfield scanning TEM (ADF-STEM) images shown in Fig. 2e, f confirm the structural continuity of our MoS₂ film grown under those conditions on the nanometre and atomic length scales. The DF-TEM image shows a continuous polycrystalline monolayer film with no visible gaps and a bilayer area of less than 0.5%. Further analysis of the DF-TEM and electron diffraction data (see Supplementary Fig. 8) confirms a uniform angular distribution of crystal orientations with no preferred intergrain tilt angle for grain boundaries. The ADF-STEM data (Fig. 2f; more images are shown in Supplementary Fig. 9) further confirm that adjacent grains are likely to be connected by a high-quality lateral connection with structures similar to those seen in previous reports^{18,19}. The MoS₂ films shown in Fig. 1 as well as those whose electrical properties we show in Figs 3 and 4 were grown under the conditions described in Supplementary Methods, producing an average grain size of ~ 1 μm (see Fig. 2b, e). Almost identical growth parameters with $P_{\text{W}} \approx 10^{-4}$ Torr produced monolayer WS₂ films as shown in Fig. 1b, i, indicating the same layer-by-layer growth for WS₂ with a similar t_0 .

The electrical properties of our monolayer MoS₂ films have two important characteristics: the spatial uniformity over a large scale and excellent transport properties similar to those seen in exfoliated samples. All our electrical measurements in Figs 3 and 4 (except those in Fig. 3c) were performed at room temperature. Figure 3a shows a plot of sheet conductance (σ_{\square}) against backgate voltage (V_{BG}) measured from a monolayer MoS₂ field-effect transistor (FET; optical image

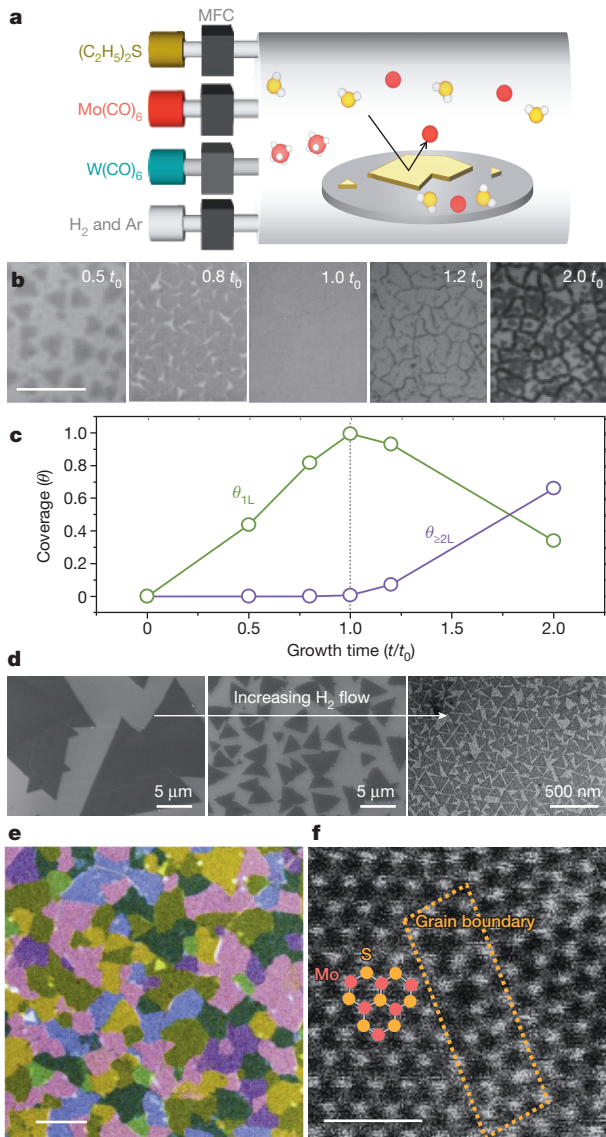


Figure 2 | MOCVD growth of continuous monolayer MoS₂ film. **a**, Diagram of our MOCVD growth setup. Precursors were introduced to the growth setup with individual mass flow controllers (MFCs). Red, Mo or W atom; yellow, S atom; white, carbonyl or ethyl ligand. **b**, Optical images of MOCVD-grown MoS₂ at the indicated growth times, where t_0 was the optimal growth time for full monolayer coverage. Scale bar, 10 μm . **c**, Coverage ratio for monolayer (θ_{1L} , green) and multi-layer ($\theta_{\geq 2L}$, purple) regions as a function of growth time. **d**, Grain size variation of monolayer MoS₂ depending on the hydrogen flow rate; from left to right, 5 standard $\text{cm}^3 \text{min}^{-1}$ (sccm) (SEM image shown), 20 sccm (SEM) and 200 sccm (TEM). **e**, False-colour DF-TEM image showing a continuous monolayer MoS₂ film. Scale bar, 1 μm . **f**, ADF-STEM image of a laterally stitched grain boundary in a monolayer MoS₂ film, with red and yellow dots representing the Mo and S atoms, respectively. Scale bar, 1 nm.

shown in the inset) with multiple electrodes for the four-probe measurements (except for a channel length L of 34 μm). It includes several curves for different L ranging between 1.6 and 34 μm (shifted from the bottom curve for clarity), all of which show nearly identical behaviours, including the n-type conductance, carrier concentration ($\sim 4 \times 10^{12} \text{cm}^{-2}$ at $V_{\text{BG}} = 0 \text{V}$) and high field-effect mobility (μ_{FE}). Figure 3b further plots μ_{FE} measured from five such devices, fabricated at random locations and separated by up to 3.3 mm on a single chip. All the devices show similar μ_{FE} near $30 \text{cm}^2 \text{V}^{-1} \text{s}^{-1}$, independent of L and device location, with similarly uniform $\sigma_{\square} - V_{\text{BG}}$ curves (shown in Supplementary Fig. 10), suggesting the spatial homogeneity of the

electrical properties of the MoS₂ film at length scales ranging from micrometres to millimetres.

The distribution of μ_{FE} of our devices is compared with the results of multiple devices from two previous reports, each measured from individual grains of exfoliated⁷ or CVD-grown²¹ MoS₂ samples. We find that μ_{FE} measured from our MOCVD film is similar to the median μ_{FE} (denoted by a star) of exfoliated samples (and several times higher than the CVD results) and has a much narrower distribution. In addition, the temperature dependence of μ_{FE} (Fig. 3c) measured from the same device in Fig. 3a shows higher μ_{FE} at lower temperatures ($92 \text{cm}^2 \text{V}^{-1} \text{s}^{-1}$ at 100 K) and intrinsic, phonon-limited electron transport similar to the behaviours previously observed in exfoliated samples (data from ref. 6 shown in Fig. 3c) but different from those observed from a CVD sample with stronger effects from defects³⁰. Specifically, our data show that the temperature dependence of mobility follows a power law of $\mu_{\text{FE}} \approx T^{-\gamma}$ with exponent $\gamma = 1.6$ for temperatures between 150 and 300 K, close to the value (1.69) predicted by theory⁵ and consistent with results from previous experiments (average value ranging between 0.6 and 1.7)^{6–9} for a similar temperature range. Finally, Fig. 3d shows a high-performance MoS₂ FET fabricated with an individual top-gate electrode (V_{TG}). It has a high on/off conductance ratio ($\sim 10^6$), current saturation at relatively low bias V_{SD} (lower inset to Fig. 3d), high field-effect mobility ($\sim 29 \text{cm}^2 \text{V}^{-1} \text{s}^{-1}$) and large transconductance ($\sim 2 \mu\text{S} \mu\text{m}^{-1}$), all of which are comparable to the best reported results^{6–8}. We note that our devices studied in Fig. 3a–d were fabricated at random locations using a polycrystalline monolayer MoS₂ film, unlike the devices with single-grain samples used for comparison. In addition, the electrical properties measured from a separate monolayer MoS₂ film with a larger average grain size of 3 μm (instead of 1 μm in Fig. 3) have almost identical characteristics, including the channel-length independence of μ_{FE} and the phonon-limited transport at $T > 150 \text{K}$ (see Supplementary Fig. 11; with the low-temperature mobility as high as $114 \text{cm}^2 \text{V}^{-1} \text{s}^{-1}$ at 90 K). Taken together, our data confirm the spatial uniformity and high electrical performance of our MoS₂ FETs independent of the average grain size, which suggests that the intergrain boundaries in our film do not significantly degrade their electrical transport properties. This is probably due to the formation of well-stitched intergrain boundaries with a low level of defects, an explanation also supported by the ADF-STEM (Fig. 2f) and X-ray photoelectron spectrum data (Supplementary Fig. 2) discussed above. Our data therefore lead us to conclude that our optimized MOCVD growth provides an electrically homogeneous monolayer MoS₂ film. Moreover, we successfully fabricated and measured 60 FETs by using a monolayer WS₂ film. Even though the growth of monolayer WS₂ was not carefully optimized, these devices showed excellent electrical properties, with their μ_{FE} as high as $18 \text{cm}^2 \text{V}^{-1} \text{s}^{-1}$ at room temperature (Fig. 3e) and a median μ_{FE} close to $5 \text{cm}^2 \text{V}^{-1} \text{s}^{-1}$. In addition, the WS₂ device in Fig. 3e showed a high on/off ratio of 10^6 and the current saturation behaviour (inset to Fig. 3e) as in our MoS₂ devices. (See Supplementary Fig. 12 for data from additional monolayer WS₂ FET devices).

The structural and electrical uniformity of our MoS₂ film enables the wafer-scale batch fabrication of high performance FETs as demonstrated in Fig. 3f, g. Figure 3f shows a photo of 8,100 MoS₂ FETs with a global back gate, which were fabricated on a 4-inch SiO₂/Si wafer with a standard photolithography process. The middle and bottom insets to Figure 3f show colour-scale maps of σ_{\square} measured from 100 MoS₂ FETs in one square region at $V_{\text{BG}} = +50 \text{V}$ and -50V , respectively; the top inset to Fig. 3f shows an enlarged optical image of the devices. We observed an almost perfect device yield of 99%; only two out of 200 FETs that we characterized (including data from an adjacent region) did not conduct. Our data also confirm the spatially uniform n-type transistor operation (larger σ_{\square} for positive V_{BG}) with similar V_{BG} dependence for all our devices and high on-state device conductance. We further observed similarly uniform V_{BG} dependence from FET devices fabricated using monolayer MoS₂ films with different average grain sizes, as characterized by the histograms of the threshold voltages

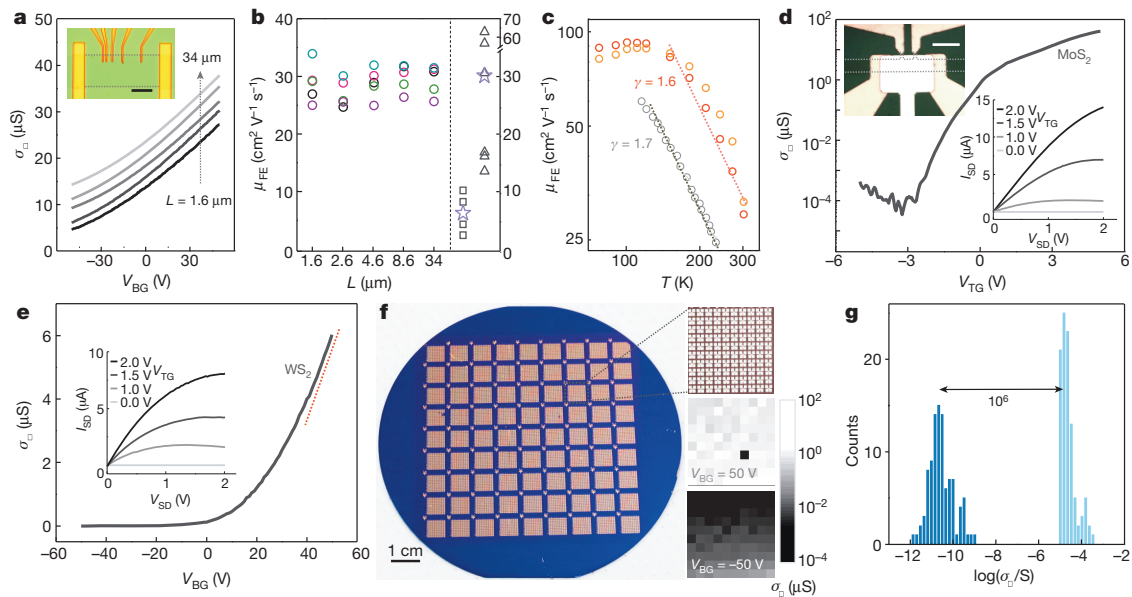


Figure 3 | Electrical characterization and batch fabrication of monolayer TMD FETs. **a**, Gate-dependent sheet conductance (σ_{\square}) of monolayer MoS₂ FETs measured at different channel lengths L (curves displaced from the bottom for clarity). Inset: optical image of the device; scale bar, 10 μm . **b**, Field-effect mobility (μ_{FE}) measured from five MoS₂ FETs (ellipses) fabricated at random locations with different L . Data from previous results for CVD-grown samples²¹ (squares) and exfoliated samples⁷ (triangles) are shown for comparison (purple stars indicate their medians). **c**, Temperature dependence of μ_{FE} measured from the device in Fig. 3a at $L = 1.6 \mu\text{m}$ (orange) and $8.6 \mu\text{m}$ (red), and from a previous report on exfoliated samples⁶ (grey), both showing phonon-limited intrinsic transport. **d**, Top gate (V_{TG})-dependent σ_{\square} for dual-gate monolayer MoS₂ FET (device shown in the upper inset). Lower inset:

V_{TG} -dependent $I_{\text{SD}}-V_{\text{SD}}$ curves showing current saturation and ohmic electrode contact. Scale bar, 10 μm . **e**, Gate-dependent σ_{\square} of a monolayer WS₂ FET showing $\mu_{\text{FE}} = 18 \text{ cm}^2 \text{ V}^{-1} \text{ s}^{-1}$. Inset: V_{TG} -dependent $I_{\text{SD}}-V_{\text{SD}}$ curves showing current saturation and ohmic electrode contact. **f**, Batch-fabricated 8,100 MoS₂ FET devices on a 4-inch SiO₂/Si wafer. Top inset: enlarged image of one square containing 100 devices. Middle and bottom insets: corresponding colour maps of σ_{\square} at gate bias $V_{\text{BG}} = 50 \text{ V}$ and -50 V , respectively, with the black block in the middle inset representing the only non-conducting device. **g**, Histogram of on-state and off-state σ_{\square} of 100 dual-gate FETs showing a median on-off ratio of 10^6 and a high on-state conductivity. Dark blue, $V_{\text{TG}} = -5 \text{ V}$; pale blue, $V_{\text{TG}} = +5 \text{ V}$. All measurements were performed at room temperatures except those in **c**.

(Supplementary Fig. 13). Similarly, we fabricated 100 individually addressable dual-gate MoS₂ FETs (similar to the device in Fig. 3d) on another wafer piece. The histogram of the on-state σ_{\square} ($V_{\text{TG}} = 5 \text{ V}$; median carrier concentration $\sim 7 \times 10^{12} \text{ cm}^{-2}$) and off-state σ_{\square} ($V_{\text{TG}} = -5 \text{ V}$) collected from all such FETs (Fig. 3g) shows strong peaks above 10^{-5} S and near 10^{-11} S , respectively, confirming a uniform conductance switching behaviour with high on-state σ_{\square} ($>10 \mu\text{S}$) and on-off ratio ($\sim 10^6$). In addition, most of these batch-fabricated FETs had a high μ_{FE} ($>10 \text{ cm}^2 \text{ V}^{-1} \text{ s}^{-1}$; see Supplementary Fig. 14).

The data presented in Figs 1–3 confirm the structural and electrical uniformity of the wafer-scale monolayer MoS₂ film grown by our MOCVD method. This makes our film compatible with batch device fabrication processes on a technologically relevant scale. Moreover, because SiO₂ provides a substrate for its growth, one can produce high-quality monolayer films on a variety of substrates by depositing SiO₂ before the growth. This versatility would permit the fabrication of high-performance FETs directly on non-conventional substrates, such as metal and thermally stable plastic. In addition, one can integrate multiple layers of MoS₂ devices by repeating the TMD film growth, device fabrication and SiO₂ deposition, which could enable novel three-dimensional circuitry.

In Fig. 4 we demonstrate this unique potential by producing multi-stacked monolayer MoS₂ films as well as electronic devices fabricated at different vertical levels. Figure 4a shows diagrams and photographs of three substrates each with single, double or triple monolayer MoS₂ films grown at different levels. The first (bottom) monolayer film was grown on a fused silica substrate; the additional layers were grown on SiO₂ (100 nm thick) deposited on the previously grown MoS₂ monolayer by using plasma-enhanced CVD. The colour of the substrate, which remains uniform for each substrate, becomes darker as the number of layers increases. Their absorption spectra, shown in Fig. 4b, present almost identical absorption at all

measured wavelengths, once normalized by the number of stacks grown (see the inset), suggesting little degradation of the optical properties of the monolayer MoS₂ films after subsequent oxide deposition and MoS₂ growth.

Figure 4c shows successive diagrams of our multi-stacked device fabrication process: growth of the first MoS₂ monolayer on a SiO₂/Si wafer, FET fabrication, deposition of SiO₂ (thickness 500 nm; see Supplementary Methods for details), and growth of the second MoS₂ monolayer and FET fabrication. A false-colour SEM image in Fig. 4d shows an array of MoS₂ FETs successfully fabricated with this process. It includes functioning MoS₂ FETs located at two different vertical levels whose conductance can be simultaneously modulated with a global back gate. The $I_{\text{SD}}-V_{\text{SD}}$ curves measured from two FETs, adjacent both laterally and vertically (see the inset to Fig. 4d), are shown in Fig. 4e. Both devices show a V_{BG} -dependent conductance change (notice the smaller change for the second layer) with an on-state σ_{\square} of 2.5 μS (first layer) and 1.5 μS (second layer), respectively. Furthermore, we measured similar μ_{FE} values (11.5 and 8.8 $\text{cm}^2 \text{ V}^{-1} \text{ s}^{-1}$) from the two devices (Supplementary Fig. 15). The two monolayer MoS₂ films were grown on SiO₂ substrates prepared differently, and the first-layer device had gone through additional steps, including the second MoS₂ growth. Our data in Fig. 4 thus confirm the compatibility of our MOCVD-grown MoS₂ films with conventional thin-film deposition and multi-stacking, which could be used to develop a three-dimensional device architecture based on TMD.

Our high-mobility monolayer TMD films can be used immediately for the batch fabrication of TMD-based integrated circuitry consisting of FETs, photodetectors and light emitting diodes, on a technologically relevant multi-inch wafer scale. In addition, because our MOCVD growth is controlled by the kinetics of precursor supply rather than specific precursor-substrate chemistry

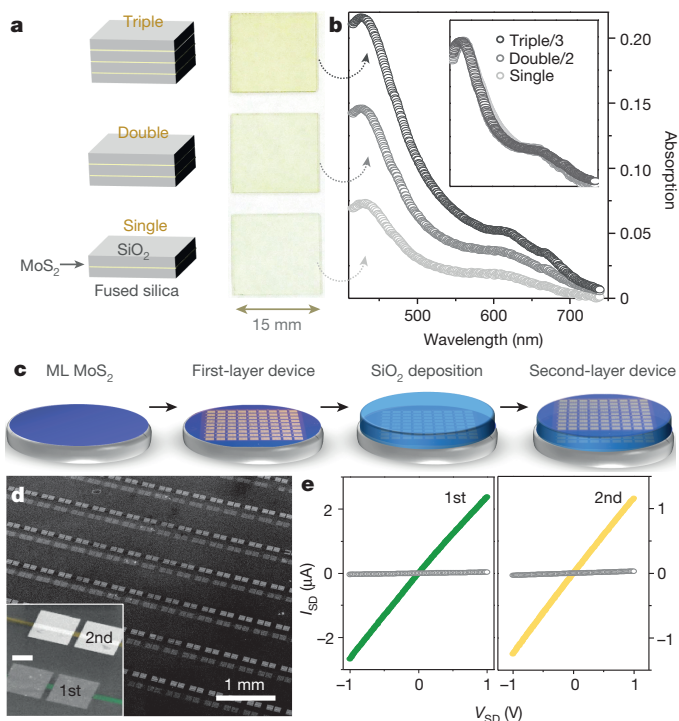


Figure 4 | Multi-stacking of MoS₂/SiO₂ structure. **a**, Diagrams (left) and optical images (right) of single, double and triple stacking of monolayer MoS₂/SiO₂. **b**, Optical absorption spectra for single, double and triple stacks, respectively (normalized spectra shown in the inset). **c**, Diagram for fabrication of MoS₂ device/SiO₂ stacking by alternating MOCVD growth, device fabrication with photolithography, and SiO₂ deposition. See the text for details. **d**, False-colour SEM image of MoS₂ FET arrays on first (bottom) and second (top) layers (the inset shows an enlarged image of a pair of devices in the same relative positions as in the main panel; scale bar, 50 μm). **e**, I_{SD} - V_{SD} curves measured from two neighbouring devices on the first (left) and second (right) layers, both showing n-type conductance switching. For the first layer, $V_{BG} = 50$ V (green) and -50 V (grey); for the second layer, $V_{BG} = 100$ V (yellow) and -100 V (grey).

(an example of the latter would be the different graphene growth modes on copper and nickel), its use is not limited to the TMD-substrate combinations reported here. Instead, it could be generalized for producing various TMD materials, both semiconductor (for example MoSe₂ or WTe₂) and metal (for example NbSe₂ or TaS₂), with precise layer control over a large scale. Indeed, our data show that, as an initial demonstration, monolayer TMD growth is possible on a variety of other technologically important substrates (such as Al₂O₃, SiN and HfO₂) with the same growth conditions as those developed for SiO₂ (see Supplementary Fig. 16 for MoS₂ growth and device fabrication on these substrates, using these non-optimized conditions). Our versatile MOCVD growth therefore provides a new avenue for the growth, patterning and integration of multiple high-quality monolayer TMD films with different compositions and electrical properties on a single substrate, enabling the future development of atomically thin integrated circuitry.

Received 25 November 2014; accepted 13 March 2015.

- Rogers, J. A., Someya, T. & Huang, Y. Materials and mechanics for stretchable electronics. *Science* **327**, 1603–1607 (2010).
- Ko, H. *et al.* Ultrathin compound semiconductor on insulator layers for high-performance nanoscale transistors. *Nature* **468**, 286–289 (2010).
- Mitzi, D. B., Kosbar, L. L., Murray, C. E., Copel, M. & Afzali, A. High-mobility ultrathin semiconducting films prepared by spin coating. *Nature* **428**, 299–303 (2003).
- Geim, A. K. & Grigorieva, I. V. Van der Waals heterostructures. *Nature* **499**, 419–425 (2013).

- Kaasbjerg, K., Thygesen, K. S. & Jacobsen, K. W. Phonon-limited mobility in n-type single-layer MoS₂ from first principles. *Phys. Rev. B* **85**, 115317 (2012).
- Baughar, B. W. H., Churchill, H. O. H., Yang, Y. & Jarillo-Herrero, P. Intrinsic electronic transport properties of high-quality monolayer and bilayer MoS₂. *Nano Lett.* **13**, 4212–4216 (2013).
- Radisavljevic, B. & Kis, A. Mobility engineering and a metal-insulator transition in monolayer MoS₂. *Nature Mater.* **12**, 815–820 (2013).
- Schmidt, H. *et al.* Transport properties of monolayer MoS₂ grown by chemical vapor deposition. *Nano Lett.* **14**, 1909–1913 (2014).
- Jariwala, D. *et al.* Band-like transport in high mobility unencapsulated single-layer MoS₂ transistors. *Appl. Phys. Lett.* **102**, 173107 (2013).
- Ovchinnikov, D. *et al.* Electrical transport properties of single-layer WS₂. *ACS Nano* **8**, 8174–8181 (2014).
- Ye, Z. *et al.* Probing excitonic dark states in single-layer tungsten disulphide. *Nature* **513**, 214–218 (2014).
- Feng, Q. *et al.* Growth of large-area 2D MoS₂(1-x)Se_{2x} semiconductor alloys. *Adv. Mater.* **26**, 2648–2653 (2014).
- Mak, K. F., Lee, C., Hone, J., Shan, J. & Heinz, T. F. Atomically thin MoS₂: a new direct-gap semiconductor. *Phys. Rev. Lett.* **105**, 136805 (2010).
- Wu, W. *et al.* Piezoelectricity of single-atomic-layer MoS₂ for energy conversion and piezotronics. *Nature* **514**, 470–474 (2014).
- Mak, K. F., McGill, K. L., Park, J. & McEuen, P. L. The valley Hall effect in MoS₂ transistors. *Science* **344**, 1489–1492 (2014).
- Lin, Y.-C. *et al.* Wafer-scale MoS₂ thin layers prepared by MoO₃ sulfuration. *Nanoscale* **4**, 6637–6641 (2012).
- Song, I. *et al.* Patternable large-scale molybdenum disulfide atomic layers grown by gold-assisted chemical vapor deposition. *Angew. Chem. Int. Ed.* **53**, 1266–1269 (2014).
- Najmaei, S. *et al.* Vapour phase growth and grain boundary structure of molybdenum disulphide atomic layers. *Nature Mater.* **12**, 754–759 (2013).
- Van der Zande, A. M. *et al.* Grains and grain boundaries in highly crystalline monolayer molybdenum disulphide. *Nature Mater.* **12**, 554–561 (2013).
- Lee, Y.-H. *et al.* Synthesis and transfer of single-layer transition metal disulfides on diverse surfaces. *Nano Lett.* **13**, 1852–1857 (2013).
- Liu, H. *et al.* Statistical study of deep submicron dual-gated field-effect transistors on monolayer chemical vapor deposition molybdenum disulfide films. *Nano Lett.* **13**, 2640–2646 (2013).
- Yu, Y. *et al.* Controlled scalable synthesis of uniform, high-quality monolayer and few-layer MoS₂ films. *Sci. Rep.* **3**, 1866 (2013).
- Zhang, Y. *et al.* Controlled growth of high-quality monolayer WS₂ layers on sapphire. *ACS Nano* **7**, 8963–8971 (2013).
- Zhao, W. *et al.* Evolution of electronic structure in atomically thin sheets of WS₂ and WSe₂. *ACS Nano* **7**, 791–797 (2013).
- Li, H. *et al.* From bulk to monolayer MoS₂: evolution of Raman scattering. *Adv. Funct. Mater.* **22**, 1385–1390 (2012).
- Berkdemir, A. *et al.* Identification of individual and few layers of WS₂ using Raman spectroscopy. *Sci. Rep.* **3**, 1755 (2013).
- King, D. A. & Woodruff, D. P. *Growth and Properties of Ultrathin Epitaxial Layers* (Elsevier, 1997).
- Connor, R. & Adkins, H. Hydrogenolysis of oxygenated organic compounds. *J. Am. Chem. Soc.* **54**, 4678–4690 (1932).
- Cristol, S. *et al.* Theoretical study of the MoS₂ (100) surface: a chemical potential analysis of sulfur and hydrogen coverage. *J. Phys. Chem. B* **104**, 11220–11229 (2000).
- Najmaei, S. *et al.* Electrical transport properties of polycrystalline monolayer molybdenum disulfide. *ACS Nano* **8**, 7930–7937 (2014).

Supplementary Information is available in the online version of the paper.

Acknowledgements We thank P. L. McEuen, M.-H. Jo, H. Heo and H.-C. Choi for discussions, and M. Guimaraes and Z. Ziegler for help in preparing the manuscript. This work was supported mainly by the AFOSR (FA2386-13-1-4118 and FA9550-11-1-0033) and the Nano Material Technology Development Program through the National Research Foundation of Korea (NRF) funded by the Ministry of Science, ICT, and Future Planning (2012M3A7B4049887). Additional funding was provided by the National Science Foundation (NSF) through the Cornell Center for Materials Research (NSF DMR-1120296) and by the Samsung Advanced Institute for Technology GRO Program. Device fabrication was performed at the Cornell NanoScale Facility, a member of the National Nanotechnology Infrastructure Network, which is supported by the National Science Foundation (ECS-0335765).

Author Contributions K.K. and S.X. contributed equally to this work. K.K., S.X. and J.P. conceived the experiments. K.K. and S.X. performed the synthesis, optical characterization, device fabrication, and electrical measurements. L.H. conducted low-temperature electrical measurement, with assistance from K.F.M., Y.H., P.Y.H. and D.A.M. performed atomic resolution STEM imaging. K.K. carried out DF-TEM and data analysis, with assistance from C.-J.K., K.K., S.X. and J.P. wrote the manuscript. All authors discussed the results and commented on the manuscript.

Author Information Reprints and permissions information is available at www.nature.com/reprints. The authors declare no competing financial interests. Readers are welcome to comment on the online version of the paper. Correspondence and requests for materials should be addressed to J.P. (jpark@cornell.edu).